

Spin transport in high-mobility graphene on WS₂ substrate with electric-field tunable proximity spin-orbit interaction

S. Omar^{1,*} and B.J. van Wees¹

¹*The Zernike Institute for Advanced Materials University of Groningen Nijenborgh 4 9747 AG, Groningen, The Netherlands*

(Dated: November 7, 2018)

Abstract

Graphene supported on a transition metal dichalcogenide substrate offers a novel platform to study the spin transport in graphene in presence of a substrate induced spin-orbit coupling, while preserving its intrinsic charge transport properties. We report the first non-local spin transport measurements in graphene completely supported on a 3.5 nm thick tungsten disulfide (WS₂) substrate, and encapsulated from the top with a 8 nm thick hexagonal boron nitride layer. For graphene, having mobility up to 16,000 cm²V⁻¹s⁻¹, we measure almost constant spin-signals both in electron and hole-doped regimes, independent of the conducting state of the underlying WS₂ substrate, which rules out the role of spin-absorption by WS₂. The spin-relaxation time τ_s for the electrons in graphene-on-WS₂ is drastically reduced down to ~ 10 ps than $\tau_s \sim 800$ ps in graphene-on-SiO₂ on the same chip. The strong suppression of τ_s along with a detectable weak anti-localization signature in the quantum magneto-resistance measurements is a clear effect of the WS₂ induced spin-orbit coupling (SOC) in graphene. Via the top-gate voltage application in the encapsulated region, we modulate the electric field by 1 V/nm, changing τ_s almost by a factor of four which suggests the electric-field control of the in-plane Rashba SOC. Further, via carrier-density dependence of τ_s we also identify the fingerprints of the D'yakonov-Perel' type mechanism in the hole-doped regime at the graphene-WS₂ interface.

Keywords: Spintronics, Graphene, graphene-semiconductor interface, spin-orbit coupling

INTRODUCTION

Recent exploration of various two-dimensional (2D) materials and their heterostructures has provided access to novel charge [1, 2] and spin-related phenomena [3–8] which are either missing or do not have a measurable effect in intrinsic graphene. Graphene (Gr) can interact with the neighboring material via weak van der Waals interactions which help to preserve its intrinsic charge transport properties while it can still acquire some foreign properties from the host substrate such as a sizable band gap in Gr-on-hexagonal Boron Nitride (hBN) substrate at the Dirac point due to a sublattice dependent crystal potential in graphene [1, 2]. For Gr-transition metal dichalcogenide (TMD) heterostructures, an enhanced intrinsic spin-orbit coupling (SOC) in the order of 5-15 meV can be induced in graphene, along with a meV order valley-Zeeman splitting due to inequivalent K and K' valleys in graphene [6, 9], a Rashba SOC due to breaking of the inversion symmetry at the graphene-TMD interface [3, 4] with a possibility of spin-valley coupling [10, 11]. This unique ability of the graphene-TMD interface makes it an attractive platform for studying the spin-related proximity induced effects in graphene.

In recent reports of spin-transport in graphene-TMD heterostructures [12, 13], a reduced spin-signal and spin-relaxation time were measured in graphene when the TMD was in conducting state. This behavior was attributed to the spin-absorption/enhanced SOC via the TMD. On the contrary, in weak anti-localization (WAL) magnetotransport measurements [5, 6], a reduced spin-relaxation time, independent of the carrier-type, carrier-density in graphene and the conducting state of the TMD was observed which was attributed to a greatly enhanced SOC in graphene via the proximity effect of the TMD. Also, the existence of the interplay between the valley-Zeeman and Rashba SOC was theoretically [11] and experimentally [14, 15] demonstrated in the anisotropy of the spin relaxation time for the out-of-plane and in-plane spin-signals in TMD-graphene heterostructures.

Surrounded by distinct conclusions, which seem to depend on the device geometry and experiment-type, it calls for revisiting the problem in a different way, i.e., a direct spin-transport measurement using TMD as a substrate for graphene. It has multiple advantages: i) similar to hBN, TMD substrates have already shown significantly improved charge transport properties of graphene [16] than graphene-on-SiO₂ due to their atomically flat and dangling-bond free surface, and screening of the charge inhomogeneities on the underlying

SiO₂ [17, 18]. This improvement can be helpful in possibly compensating for the reduced τ_s due to the enhanced SOC/ spin-absorption [12, 13], and improve the spin-signal magnitude, ii) due to partial encapsulation of graphene with the TMD [13–15], the encapsulated and non-encapsulated graphene regions have different charge and spin-transport properties. It requires a complex analysis for the accurate interpretation of the TMD induced spin-relaxation in graphene. On the other hand, spin-transport measurements in graphene fully supported on a TMD substrate do not have this drawback and can distinguish the possible effects of spin-absorption via the TMD or a proximity-induced SOC, due to a uniform carrier density and identical effect of the substrate present everywhere in graphene, and iii) in contrast with the TMD-on-graphene geometry [12–15] where graphene partially shields the back-gate induced electric field to the TMD, and one cannot clearly comment on the TMD’s conducting state and correlate its effect on spin-transport in graphene, the inverted Gr-on-TMD geometry does not have this drawback. Lastly, it is worth exploring the possibility of recently observed spin-relaxation anisotropy for in-plane and out-of-plane spins in Gr-TMD heterostructures [11, 14, 15] in our system.

We study the charge and spin-transport properties of graphene, fully supported on a tungsten disulfide (WS₂) substrate, and partially encapsulated with a top hBN flake, using a four-probe local and non-local geometry, respectively. We measure large values of charge mobility up to 16,000 cm²V⁻¹s⁻¹. For spin-valve measurements, the obtained spin-signal ΔR_{NL} is almost constant and independent of the carrier type and carrier density in graphene, ruling out the possibility of spin-absorption via the underlying WS₂ substrate. For Hanle measurements, we obtain a very low spin-relaxation time $\tau_s \sim 10$ ps in the electron-doped regime than $\tau_s \sim 800$ ps of a reference graphene flake on the SiO₂/Si substrate in the same chip. Via the top-gate voltage application, we can access the hole doped regime of graphene in the encapsulated region where τ_s is enhanced up to 40-80 ps for various carrier densities and electric fields. By changing the electric-field in the range of 1 V/nm in the encapsulated region, we can change τ_s from 20-80 ps, almost by factor of four, which suggests an electric-field controlled Rashba SOC in our system [9, 19]. For both electron and hole regimes (stronger for the hole regime), we observe the fingerprints of the D’yakonov-Perel’ type mechanism for spin-relaxation, similar to WAL measurements [3, 4]. For Gr-on-WS₂, the ratio of the out-of-plane to the in-plane ΔR_{NL} (therefore τ_s) in the electron-doped regime is less than one, an indicative of an in-plane Rashba-type system [11, 20]. For the

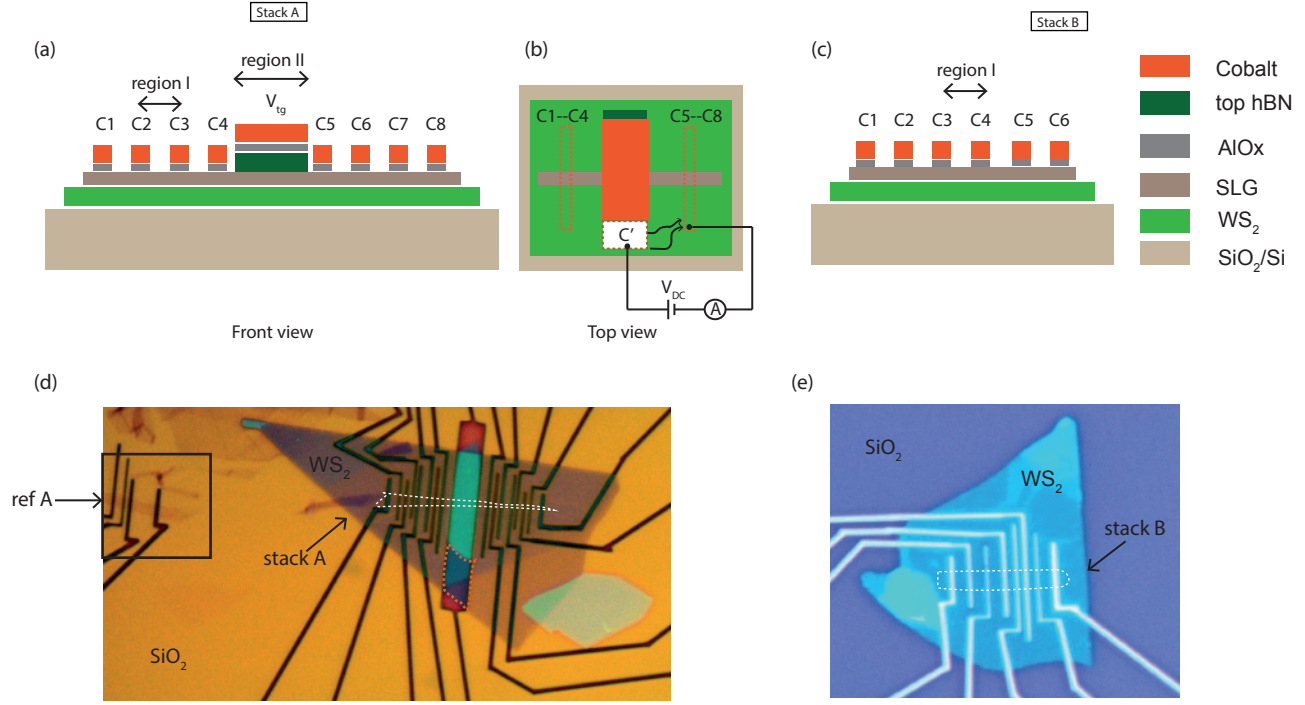


FIG. 1. (a) Stack A: a hBN/Gr/WS₂ stack with Co/AIO_x ferromagnetic (FM) tunnel contacts and a top gate. (b) Top-view of stack A. White region marked by C' represents the top-gate electrode contacting the WS₂ substrate. The connection scheme for measuring the $I - V$ behavior of WS₂ is also shown. (c) Stack B: graphene supported on a bottom WS₂ substrate. (d) Optical image of stack A before the contact deposition. The graphene flake is outlined by a white dotted line, and the orange dotted line denotes the WS₂ flake region to be contacted by the top-gate electrode after the contact deposition. On the top left corner outlined with a black square, a graphene flake (ref A) with the developed contacts can be seen on the same SiO₂/Si substrate. (e) Optical image of stack B, i.e., a graphene (white dashed lines)/WS₂ heterostructure after the contact deposition. It also has a reference Gr flake 'ref B' on the same SiO₂ substrate (not shown in the image).

hole doped regime, we observe an enhanced out-of-plane spin-signal [15] which suggests a higher τ_s^\perp for the out-of-plane spins. However, in the presence of a similar background magnetoresistance signal, the anisotropic behavior can not be uniquely determined and requires further measurements [14, 15].

We also confirm the signature of WS₂ induced SOC in graphene-on-WS₂ by measuring the WAL signature, similar to the studies performed in refs. [3–6]. Therefore, a low τ_s in

graphene-on-WS₂ substrate, with an electric-field tunable Rashba SOC and a WAL signature in the same sample can be attributed to the WS₂ induced proximity SOC at the graphene-WS₂ interface.

DEVICE FABRICATION

The graphene-WS₂ stacks are prepared on a n⁺⁺-doped SiO₂/Si substrate ($t_{\text{SiO}_2} \sim 300$ nm) via a dry pick-up transfer method [7, 21]. The WS₂ flake is exfoliated on a polydimethylsiloxane (PDMS) stamp and identified using an optical microscope. The desired flake is transferred onto a pre-cleaned SiO₂/Si substrate ($t_{\text{SiO}_2}=300$ nm), using a transfer-stage. The transferred flake on SiO₂ is annealed in an Ar-H₂ environment at 250°C for 3 hours in order to achieve a clean top-WS₂ surface. The graphene (Gr) flake is exfoliated from a ZYB grade HOPG (Highly oriented pyrolytic graphite) crystal and boron nitride (BN) is exfoliated from BN crystals (size ~ 1 mm) onto different SiO₂/Si substrates ($t_{\text{SiO}_2}=300$ nm). Both crystals were obtained from HQ Graphene. The desired single layer graphene and hBN flakes are identified using the optical microscope. In order to prepare an hBN/Gr/WS₂ stack, first the hBN flake is picked up by a polycarbonate (PC) film attached to a PDMS stamp, using the same transfer-stage. Next, the Gr flake is aligned with respect to the hBN flake. When graphene is brought in a contact with the hBN flake, the graphene region underneath the hBN flake is picked up by the van der Waals force between the two flakes. The graphene region outside the hBN flake is picked up by the sticky PC film. Now the WS₂ flake, previously transferred onto a SiO₂/Si substrate, is aligned and brought in a contact with the PC/hBN/Gr assembly and the whole system is heated up to 150°C, so that the PC/hBN/Gr assembly is released onto the WS₂ substrate. Now, the stack is put in a chloroform solution for 3 hours in order to remove the PC film used in the stack preparation. After that, the stack is annealed again in the Ar-H₂ environment for five hours at 250°C to remove the remaining polymer residues. The thicknesses of WS₂ and BN flakes were characterized by the Atomic Force Microscopy measurements.

In order to define the contacts, a poly-methyl methacrylate (PMMA) solution is spin-coated over the stack and the contacts are defined via the electron-beam lithography (EBL). The PMMA polymer exposed via the electron beam gets dissolved in a MIBK:IPA (1:3) solution. In the next step, 0.7 nm Al is deposited in two steps, each step of 0.35 nm followed

by 12 minutes oxidation in an oxygen environment to form a AlO_x tunnel barrier. On top of it, 70 nm thick cobalt (Co) is deposited to form the ferromagnetic (FM) tunnel contacts with a 3 nm thick Al capping layer to prevent the oxidation of Co electrodes, followed by the lift-off process in acetone solution at 30°C.

RESULTS

We study two samples: i) stack A: a hBN/Gr/WS₂ stack consisting of a single layer graphene encapsulated between a bottom-WS₂ ($t_{\text{WS}_2} \sim 3.5$ nm) and a top-hBN ($t_{\text{hBN}} \sim 8$ nm) flake, as shown in Figs. 1(a,b,d) and ii) stack B: a WS₂/Gr stack consisting of a single layer graphene supported on a bottom WS₂ flake ($t_{\text{WS}_2} \sim 4.2$ nm), without any hBN encapsulation from the top, as shown in Figs. 1(c,e). On the same SiO₂/Si chip, there are reference graphene flakes near stack A (Fig. 1(d)) and stack B. Therefore, we can directly compare the charge and spin-transport properties of the reference Gr flakes on SiO₂ and graphene-on-WS₂ substrate, prepared via identical steps. The reference flakes on the same SiO₂, shared by stack A and stack B, are labeled as ‘ref A’ and ‘ref B’ respectively. Moreover, stack A has non-encapsulated regions (region-I) and an encapsulated region (region-II) both, as indicated in the device schematic of Fig. 1(a). On the other hand, stack B only consists of region-I. Therefore, we will discuss the data of stack A as a representative device.

We use a low-frequency lock-in detection method to measure the charge and spin transport properties of the graphene flake. In order to measure the I-V behavior of the WS₂ flake and for gate-voltage application, a Keithley 2410 dc source meter was used. All measurements are performed at room temperature and at 4 K under the vacuum conditions in a cryostat.

Charge transport measurements

We measure the charge transport via the four-probe local measurement scheme. For measuring the gate-dependent resistance, i.e., the Dirac behavior of graphene-on-WS₂ in region-I (II) of stack A, a fixed ac current $i_{\text{ac}} \sim 100$ nA is applied between contacts C1-C4 (C1-C6) and the voltage-drop is measured between contacts C2-C3 (C4-C5), while the back-gate (top-gate) voltage is swept. The maximum resistance point in the Dirac curve is denoted as the charge neutrality point (CNP). For graphene-on-WS₂, it is possible to

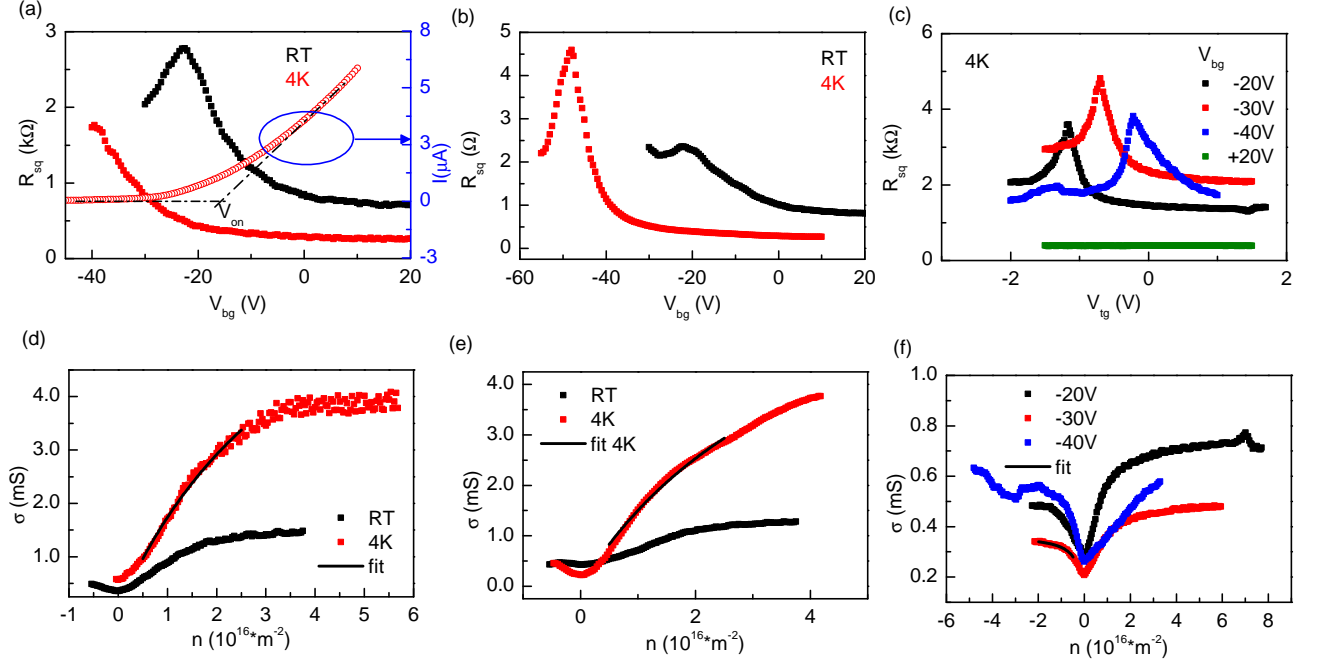


FIG. 2. (a) For region-I of stack A, the $R_{\text{sq}} - V_{\text{bg}}$ dependence at RT and 4 K is shown on the left axis. The $I_{\text{DS}} - V_{\text{bg}}$ behavior of WS_2 at 4 K is shown on the right-y axis (open circle). For region-II (b) the $R_{\text{sq}} - V_{\text{bg}}$ and (c) the $R_{\text{sq}} - V_{\text{tg}}$ behavior of Gr encapsulated between WS_2 and hBN flakes. The corresponding $\sigma - V_{\text{bg(tg)}}$ behaviors are plotted in (d), (e) and (f).

tune the Fermi energy E_{F} in graphene until E_{F} lies within the band-gap of WS_2 . After E_{F} coincides with the conduction band edge of WS_2 , it also starts conducting, and V_{bg} corresponding to this transition is denoted as V_{on} . For $V_{\text{bg}} > V_{\text{on}}$, the WS_2 flake screens the electric field from the back-gate due to a charge accumulation at the SiO_2 - WS_2 interface [5] and the resistance of the graphene flake cannot be further modified via V_{bg} .

The Dirac curves for region-I and region-II of stack A are shown as a function of V_{bg} in Fig 2(a) and Fig 2(b), respectively. The same is also shown as a function of top-gate voltage V_{tg} in region-II in Fig. 2(c). In order to extract the carrier mobility μ , we fit the charge-conductivity σ versus carrier density n plot with the following equation:

$$\sigma = \frac{1}{R_{\text{sq}}} = \frac{ne\mu + \sigma_0}{1 + R_{\text{s}}(ne\mu + \sigma_0)}. \quad (1)$$

Here R_{sq} is the square resistance of graphene, σ_0 is the conductivity at the CNP, R_{s} is the residual resistance due to short-range scattering [21–23] and e is the electronic charge. We

fit the $\sigma - n$ data for n (both electrons and holes) in the range $0.5-2.5 \times 10^{12} \text{ cm}^{-2}$ with Eq. 1. For the non-encapsulated region we obtain the electron-mobility $\mu_e \sim 9,700 \text{ cm}^2\text{V}^{-1}\text{s}^{-1}$ at room temperature (RT), which is enhanced up to $13,400 \text{ cm}^2\text{V}^{-1}\text{s}^{-1}$ at 4 K (Fig. 2(d)). For the encapsulated region, we extract a relatively lower $\mu_e \sim 7,300 \text{ cm}^2\text{V}^{-1}\text{s}^{-1}$ at RT which is enhanced at 4 K up to $11,500 \text{ cm}^2\text{V}^{-1}\text{s}^{-1}$ (Fig. 2(e)). Via the top gate voltage application, we can access the hole carrier densities up to $\sim -7 \times 10^{16} \text{ cm}^{-2}$, and extract the hole mobility μ_h at different V_{bg} values in the range $12,600-16,000 \text{ cm}^2\text{V}^{-1}\text{s}^{-1}$ at 4 K (Fig. 2(f)). Via this analysis, we get $\mu_e \sim 6,000-13,000 \text{ cm}^2\text{V}^{-1}\text{s}^{-1}$ at different V_{bg} values, similar to values that were extracted from the back-gate sweep in Fig. 2(e).

In order to obtain the transfer characteristics of the WS_2 substrate, we use a specific measurement geometry. Due to partial encapsulation of the bottom- WS_2 via the top-hBN layer, as marked by the orange dashed lines in Fig. 1(d), the WS_2 crystal is contacted via the top gate electrode (white region in Fig. 1(b), labeled as C') and one of the electrodes C1-C8 on the graphene flake. For a voltage applied between C' and C_j ($j = 1 - 8$), there is a current flowing through WS_2 , as schematically indicated by arrows in Fig. 1(b). The $I_{\text{DS}} - V_{\text{bg}}$ transfer curve for WS_2 measured using this geometry is plotted in Fig. 2(a) (marked by blue ellipse). It is also noteworthy that there is a negligible gating action in graphene from the top gate when the WS_2 is conducting at $V_{\text{bg}} = +20 \text{ V}$ (Fig. 2(c)).

In conclusion, for graphene-on- WS_2 , we obtain high electron and hole mobilities reaching up to $16,000 \text{ cm}^2\text{V}^{-1}\text{s}^{-1}$. We obtain similar mobilities for both encapsulated and the non-encapsulated regions, implying that the observed high mobility is due to a clean Gr- WS_2 interface in our samples, and is not significantly affected by the lithographic process during the sample preparation.

Spin-transport measurements

A nonlocal four-probe connection scheme is used to measure the spin-transport in graphene. In order to measure the spin signal ΔR_{NL} in the non-encapsulated(encapsulated) region, i_{ac} is applied between contacts C2-C1(C4-C1) and the nonlocal voltage v_{NL} is measured between C3-C8(C5-C8), in Fig. 1(a) [24].

For spin-valve measurements, first an in-plane magnetic field $B_{\parallel} \sim 0.2 \text{ T}$ is applied along the easy axes of the ferromagnetic (FM) electrodes, so that they have their magnetization

aligned in the same direction. The FM contacts are designed with different widths, therefore they have different coercivities. Now, B_{\parallel} is swept in the opposite direction, and depending on their coercivities, the FM contacts reverse their magnetization direction along the applied field, one at a time. This magnetization reversal appears as a sharp transition in v_{NL} or in the nonlocal resistance $R_{\text{NL}} = v_{\text{NL}}/i_{\text{ac}}$, as shown in Figs. 3(a) and 5(a). The spin-signal is $\Delta R_{\text{NL}} = \frac{R_{\text{NL}}^{\text{P}} - R_{\text{NL}}^{\text{AP}}}{2}$, where $R_{\text{NL}}^{\text{P(AP)}}$ represents the R_{NL} value of the two level spin-valve signal, corresponding to the parallel (P) and anti-parallel (AP) magnetization of the FM electrodes.

For Hanle spin-precession measurements, first the FM electrodes are magnetized in the parallel (P) or anti-parallel (AP) configuration. Next, for a fixed P (AP) configuration, an out-of-plane magnetic field B_{\perp} is applied and the injected spin-accumulation precesses around the applied field with the Larmor frequency $\vec{\omega}_{\text{L}} = \frac{g\mu_{\text{B}}}{\hbar} B_{\perp}$, while diffusing towards the detector, and gets dephased. Here g is the gyromagnetic ratio(=2) for an electron, μ_{B} is the Bohr magneton and \hbar is the reduced Planck constant. The measured Hanle curves are fitted with the steady state solution to the one-dimensional Bloch equation [24]:

$$D_{\text{s}} \nabla^2 \vec{\mu}_{\text{s}} - \frac{\vec{\mu}_{\text{s}}}{\tau_{\text{s}}} + \vec{\omega}_{\text{L}} \times \vec{\mu}_{\text{s}} = 0 \quad (2)$$

with the spin diffusion constant D_{s} , spin relaxation time τ_{s} and spin-accumulation $\vec{\mu}_{\text{s}}$ in the transport channel. The spin diffusion length λ_{s} is $\sqrt{D_{\text{s}}\tau_{\text{s}}}$.

Hanle measurements for ref A sample are shown in Fig. 3(d). Since we do not observe the CNP, we could only measure the spin-transport only in the electron-doped regime and obtain $D_{\text{s}} \sim 0.02 \text{ m}^2\text{s}^{-1}$ and τ_{s} in the range 730-870 ps, i.e., $\lambda_{\text{s}} \sim 3.6\text{-}3.8 \text{ }\mu\text{m}$.

After obtaining the spin-transport parameters for ref A, we measure the spin-transport in graphene-on- WS_2 substrate (region I of stack A) on the same chip. For a varying range of carrier density in graphene, from electron to hole regime with the application of V_{bg} , we measure almost a constant spin signal ΔR_{NL} at RT via spin-valve measurements, plotted in Fig. 3(b). At 4 K, the spin signal shows a modest increase around the CNP, and then it decreases. For $V_{\text{bg}} < -30 \text{ V}$, there is a negligible in-plane charge conduction in WS_2 (Fig. 2(a)). If the spin-absorption via WS_2 was the dominant spin-relaxation mechanism, the spin-signal should enhance for $V_{\text{bg}} < -30 \text{ V}$. Both observations cannot be explained by considering the gate-tunable spin-absorption as a dominant source of spin-relaxation at the graphene- WS_2 interface within the applied V_{bg} range.

Now we perform spin-valve measurements in the encapsulated region (region-II of stack

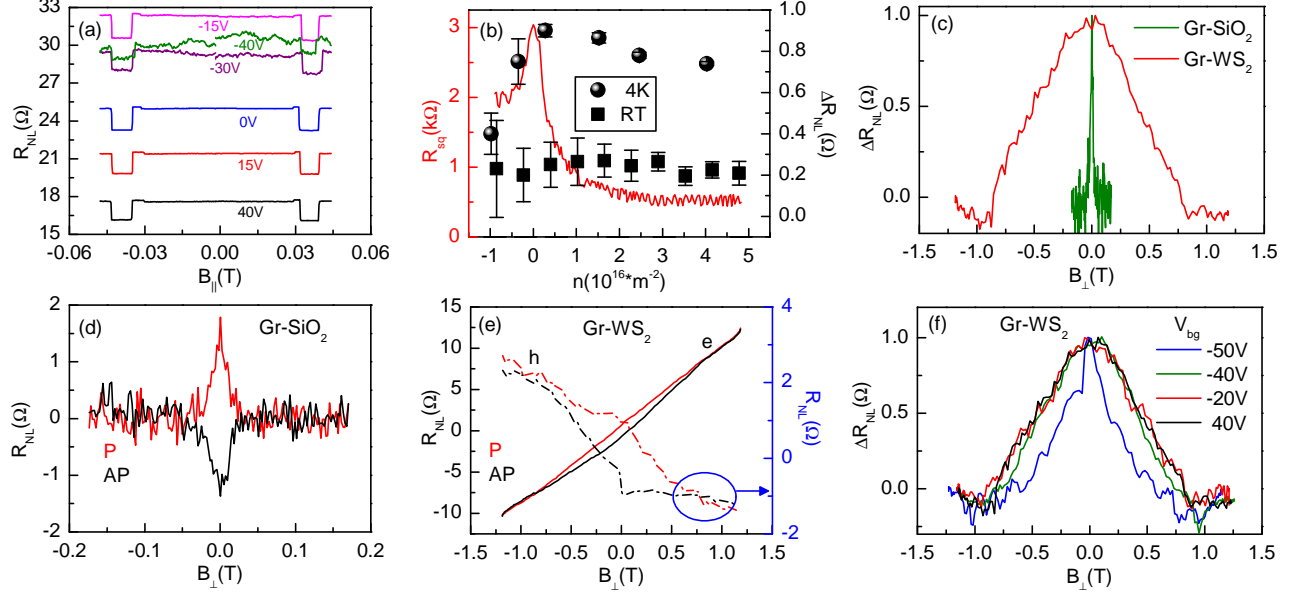


FIG. 3. (a) Spin-valve measurements for Gr-on-WS₂ (region-I of stack A) at different V_{bg} for the injector-detector separation $L=0.8 \mu\text{m}$, and the corresponding (b) ΔR_{NL} as a function of carrier density in graphene at RT and 4 K. (c) Normalized Hanle signal $\Delta R_{NL}(B_{\perp})$ for graphene-on-SiO₂ (green) and on-WS₂ (red) at 4 K. (d) Parallel (P) and anti-parallel (AP) Hanle signals R_{NL} for graphene-on-SiO₂ and (e) for graphene-on-WS₂ (region-I of stack A). A large linear background can also be seen in both P and AP configurations and in electron and hole-doped regimes. (f) $\Delta R_{NL}(B_{\perp})$ in region-I of stack A at different V_{bg} at 4 K.

A), as a function of V_{bg} and V_{tg} (Fig. 5(a)). For a wide range of carrier density in the encapsulated graphene which is equivalent to applying V_{bg} in the range of ± 60 V, we do not see any significant change in the spin-signal in Fig. 5(a), similar to the back-gate dependent spin-valve measurements (Fig. 3(a)). It leads to a conclusion that ΔR_{NL} is independent of the carrier density, carrier type in graphene and the conducting state of the TMD. Note that this configuration is similar to the TMD-on-graphene configuration with a back gate application in ref.[12, 13], except graphene is uniformly covered with the WS₂ flake in our sample.

In order to estimate λ_s from spin-valve measurements in region-I, we measure ΔR_{NL} at different injector-detector separation L values. Assuming equal polarization p for all the

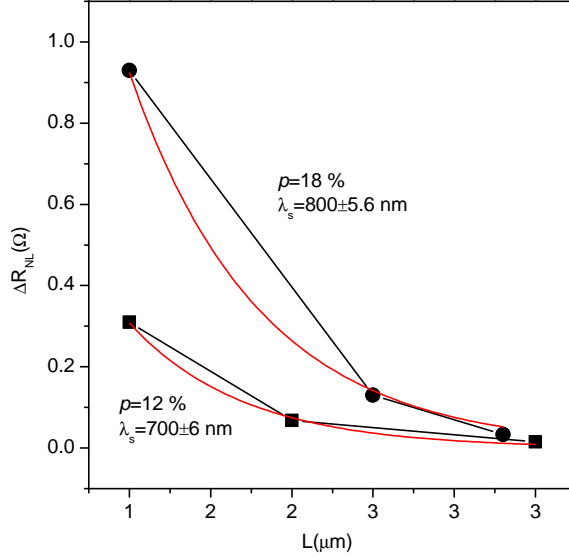


FIG. 4. Exponentially decaying spin signal ΔR_{NL} in stack A (region-I) for an increasing injector-detector separation L . Black square and circle data points are taken for two different injector electrodes. Here, we assume equal spin-polarization for all the contacts. The data is fitted using Eq. 3.

contacts, we can estimate λ_s using the relation [24]:

$$\Delta R_{\text{NL}} = \frac{p^2 R_{\text{sq}} \lambda_s e^{-\frac{L}{\lambda_s}}}{2w} \quad (3)$$

where w is the width of the spin-transport channel. We obtain λ_s around 700-800 nm (Fig. 4), which is almost five times lower than λ_s in ref A sample. For graphene-on- WS_2 , we obtain the charge diffusion coefficient $D_c \sim 0.05 \text{ m}^2\text{s}^{-1}$ using the Einstein relation: $\sigma = e^2 D_c \nu$, where ν is the density-of-states in graphene. Assuming $D_s = D_c$ [20], we estimate $\tau_s \sim 10 \text{ ps}$, using λ_s obtained from spin-valve measurements (Fig. 4). Note that this value may be uncertain due to different polarization values of the individual contacts, still it gives an estimate of λ_s [25].

In region-I of stack A, we measure broad Hanle curves with full-width half maximum in the range of $\sim 1 \text{ T}$ (Figs. 3(c),(e), (f)). A direct comparison between Hanle curves of the reference sample and for graphene-on- WS_2 , plotted together in Fig. 3(c), clearly demonstrates the effect of the WS_2 substrate in the broadening of the Hanle curve. The line shape of ΔR_{NL} remains similar at different carrier densities ($n \sim 0.6 \times 10^{16} \text{ m}^{-2}$) in the

electron-doped regime (Fig. 3(f)). Note that the WS_2 gets switched on around the CNP of the graphene and remains in the conducting-state in this regime. By using the Hanle curve fitting procedure, we obtain $\tau_s \sim 10\text{-}13$ ps and $D_s \sim 0.03\text{-}0.04$ m^2s^{-1} which matches with D_c within factor of two obtained from the charge transport measurements. With the obtained D_s and τ_s via the Hanle measurements, we achieve $\lambda_s \sim 600\text{-}700$ nm, using $\lambda_s = \sqrt{D_s\tau_s}$, in a good-agreement with λ_s obtained from the distance-dependence of spin-valve measurements. In the hole transport regime, we could perform the Hanle measurements only at $V_{\text{bg}} = -50\text{V}$ ($D_s \sim 0.35$ m^2s^{-1} , $\tau_s \sim 35$ ps) with D_s and D_c (~ 0.03 m^2s^{-1}) differing by an order of magnitude. Therefore, we cannot comment on the spin-transport parameters in the hole transport regime in region-I.

It should be noted that at high out-of-plane magnetic fields $B_{\perp} \sim 1$ T, the magnetization direction of the FM electrodes does not fully lie in the sample-plane and makes an angle with the plane [20]. When we correct the measured data for the angular (B_{\perp}) dependence of the magnetization (not shown here) using the procedure in ref.[26], the ‘corrected’ Hanle curves become even broader. From these Hanle curves, we would obtain even lower τ_s . Therefore, the τ_s values reported here represent the upper bound.

We estimate the contact polarization $p \sim 15\text{-}20$ % using Eq. 3 for this device which along with a reasonably good $D_s \sim 0.04$ m^2s^{-1} , enables us to measure a large ΔR_{NL} in the order of Ohms, even with such a short τ_s . For stack B, we obtain a small $p \sim 1\text{-}3\%$ and therefore a small $\Delta R_{\text{NL}} \sim 7$ m Ω , making it difficult to measure clear Hanle signals at high magnetic fields in the presence of a large linear background.

For individual Hanle curves measured in P or AP configuration, we also observe a large linear background signal ($\sim 10\text{-}20$ Ω) along with the Hanle signal (Fig. 3(e)). The sign of the background-slope changes with respect to the change in the carrier-type from electrons to holes, similar to a Hall-like signal [27]. However, we do not expect such a large Hall background because the FM electrodes are designed across the width of the graphene flake. The source of such background is non-trivial and at the moment is not clear to us.

DISCUSSION

In graphene, there are two dominant spin-relaxation mechanisms [28–30] : 1) Elliot-Yafet (EY) mechanism where an electron-spin is scattered during the interaction with the

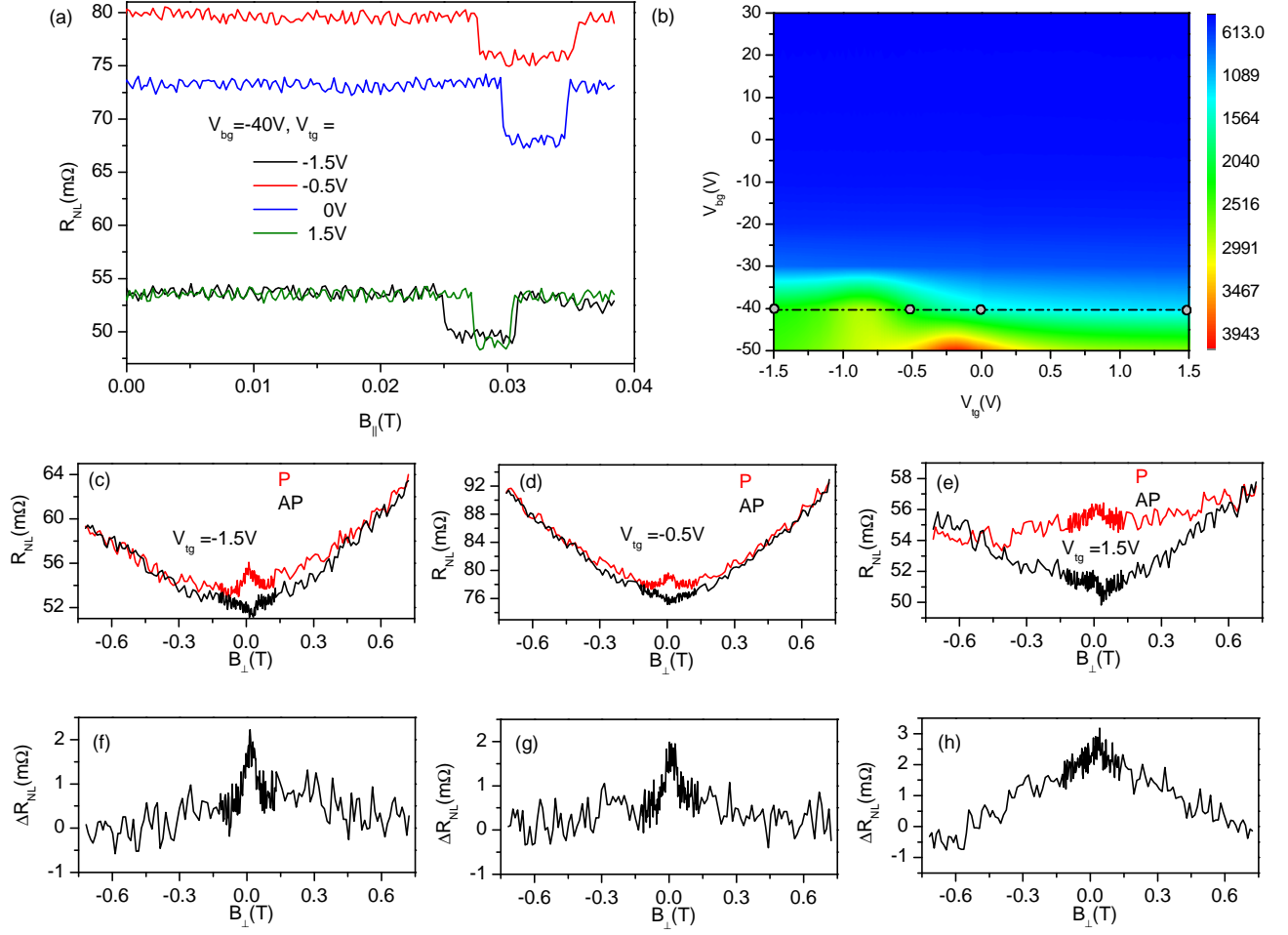


FIG. 5. (a) Spin-valve measurements across the encapsulated region (region-II) of stack A at different top-gate voltages, changing the carrier-density of the encapsulated region from hole to electron-doped regime. (b) A contour-plot of R_{sq} for the encapsulated region as a function of V_{bg} and V_{tg} . The gray circles on the horizontal dotted line at $V_{bg} = -40$ V denote the V_{tg} values at which spin valve and Hanle measurements are taken. Hanle measurements for the encapsulated region for the hole doped regime, at the CNP and electron-doped regime are shown in (c), (d) and (e), respectively. The corresponding Hanle signals are shown in (f), (g) and (h).

impurities. Therefore, the spin-relaxation time is proportional to the momentum relaxation time τ_p , i.e., $\tau_s \propto \tau_p$, 2) D'yakonov-Perel' (DP) mechanism, where the electron-spin precesses in a spin-orbit field between two momentum scattering events, following the relation $\tau_s \propto \frac{1}{\tau_p}$.

In order to check the relative contribution of the EY and DP mechanisms in our samples, we plot the τ_s versus τ_p dependence. Here, τ_p is calculated from the diffusion coefficient

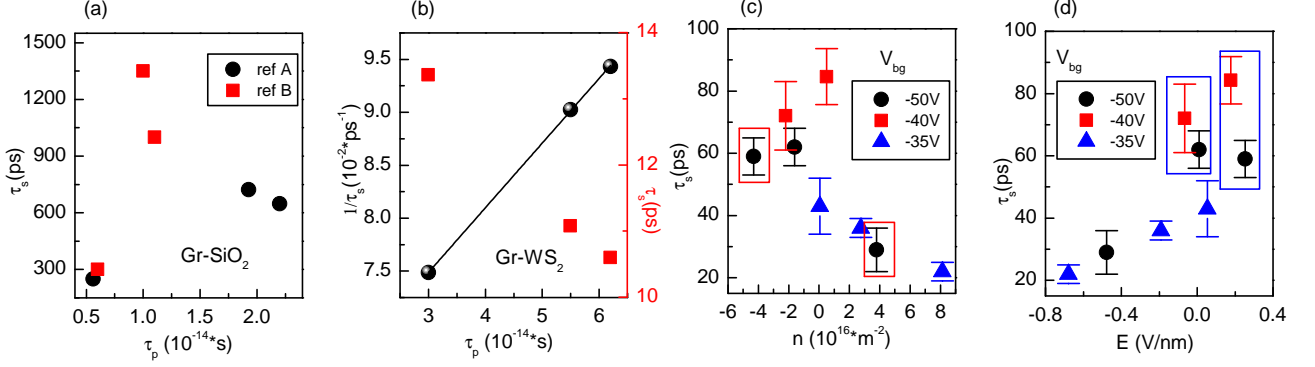


FIG. 6. (a) τ_s versus τ_p for the reference graphene on SiO_2 substrate in the electron doped-regime shows an enhanced τ_s with the increase in τ_p , suggesting the EY-type spin-relaxation. (b) τ_s versus τ_p (red squares) for graphene-on- WS_2 substrate (region-I of stack A) shows an enhanced τ_s for a reduced τ_p , suggesting the DP-type spin relaxation in presence of a substrate induced SOC. Black line represents a linear fit of $1/\tau_s - \tau_p$ data (black spheres). (c) τ_s as a function of carrier density n and (d) Electric field E at different values of V_{bg} for the electron and hole transport regime in region-II of stack A. E and n in the encapsulated-region due to a combined effect of the top and bottom gates are calculated by following the procedure in ref. [20].

D , using the relation $D \sim v_F^2 \tau_p$, assuming $D = D_s(D_c)$. For reference samples on the SiO_2 substrate, τ_s increases with τ_p in the electron doped regime (Fig. 6(a)), suggesting the dominance of the EY-type spin relaxation in single layer graphene on the SiO_2 substrate, similar to previous observations [25, 29, 30] on this system. We could not quantify the spin-orbit strength due to unknown carrier density and the corresponding Fermi energy [31]. For stack A (region-I), processed in identical conditions, we observe an opposite trend between τ_s and τ_p in the electron-doped regime (Fig. 6(b)), which resembles the DP type mechanism. We fit the data with the relation $\frac{1}{\tau_s} = \frac{4\lambda_R^2}{\hbar^2} \tau_p$ [4] and extract the Rashba SOC strength $\lambda_R \sim 250 \mu\text{eV}$, which is 4 to 6 times higher than the spin orbit coupling strength in a similar mobility graphene-on-hBN substrate reported in ref. [31], and distinguishes the effect of WS_2 substrate in enhancing the SOC in graphene. The obtained magnitude of λ_R is of similar order as reported in refs. [4, 6, 9, 11]. However, a slight variation in τ_s can drastically change the $\tau_s - \tau_p$ dependence and thus the value of λ_R . Therefore, such a small variation of the spin-relaxation rate (τ_s^{-1}) from 75 ns^{-1} to 95 ns^{-1} restricts us from claiming the dominance of the DP spin-relaxation via this analysis.

Now we perform Hanle spin-precession measurements in the encapsulated graphene ($L \sim 6.7 \mu\text{m}$ region-II of stack A). Due to the partial encapsulation of WS_2 via hBN (Fig. 1(b),(d)), we can study the effect of the top-gate on the spin-transport only when the bottom- WS_2 does not conduct. For a fixed $V_{\text{bg}} < -30\text{V}$, we can access both electron and hole regimes via the top gating. Hanle measurements shown in Figs. 5(c)-(h) at $V_{\text{bg}}=-40 \text{ V}$ correspond to the CNP of the back-gated graphene, while varying V_{tg} from the hole-doped regime at $V_{\text{tg}}=-1.5 \text{ V}$ to the electron-doped regime at $V_{\text{tg}}=+1.5 \text{ V}$. Here, we can control the carrier-density and electric field in the encapsulated region. An out-of-plane electric field breaks the $z \leftrightarrow -z$ inversion symmetry in graphene and modifies the in-plane Rashba SOC [20, 32, 33]. For the hole regime at $V_{\text{tg}}=-1.5 \text{ V}$ (Figs. 5(c),(f)) and -0.5 V (Figs. 5(d),(g)), we measure a narrow Hanle shape, an indicative of a higher τ_s for the hole spins. Now, at $V_{\text{tg}}=+1.5 \text{ V}$, when the encapsulated region is in the electron-doped regime, the broad Hanle corresponding to a lower τ_s appears (Figs. 5(e),(h)). This feature is consistent with broad Hanle curves measured in the electron-doped regime of region-I (Figs. 3(c),(e),(f)). We fit the Hanle data in the hole-doped regime for $|B_{\perp}| < 200 \text{ mT}$, while assuming $D_s = D_c$, where D_c is obtained from the $\sigma - V_{\text{tg}}$ dependence in Figs. 2(f), and obtain $\tau_s \sim 40\text{-}80 \text{ ps}$. We repeat the Hanle measurements for $V_{\text{bg}}=-50 \text{ V}, -35 \text{ V}$ and observe a similar behavior, confirming that the hole and electron spins have different τ_s values with $\tau_s^{\text{h}} > \tau_s^{\text{e}}$ (Fig. 6(c)), where superscripts h and e refer to holes and electrons, respectively. By modulating E_{\perp} in the range of 1 V/nm , we can change τ_s almost by factor of four, which demonstrates the effective control of electric field in changing the SOC, and therefore τ_s at the Gr- WS_2 interface [9, 19].

A higher τ_s^{h} in the encapsulated region is possibly due to a combined effect of an intrinsically reduced spin-orbit coupling in the hole regime [11, 19] and modification of the electric-field induced Rashba SOC [3, 4, 20]. This can be seen in two features evident from Fig. 6(c) and Fig. 6(d). First, for a similar carrier density magnitude in the electron and hole regime, a reduced τ_s is observed in the electron-doped regime. Here, the electric field E is pointing towards WS_2 , i.e., $E < 0$ (red box in Fig. 6(c)). Second, for the same electric field an enhanced τ_s is observed at lower carrier densities (blue box in Fig. 6(d)), similar to that obtained from the WAL experiments in refs. [3, 6]. These observations support the presence of a DP type spin-relaxation mechanism for the hole transport and an electric field controllable SOC at the graphene- WS_2 interface.

Recently an anisotropic spin-relaxation, i.e., a higher τ_s for the spins oriented perpen-

dicular to the graphene plane than in the graphene plane ($\tau_s^\perp > \tau_s^\parallel$) in graphene-TMD heterostructures was theoretically predicted by Cummings *et al.* [11] and was subsequently experimentally demonstrated [14, 15]. In order to check this possibility in our system, we subtract the linear background (Figs. 3(e)) from the measured Hanle data for region-I. In the electron-doped regime, the out-of-plane to in-plane spin signal ratio is always less than one, implying $\tau_s^\perp < \tau_s^\parallel$. It could be due to the presence of a dominant in-plane Rashba SOC [20] in our system. However, in the hole-doped regime of region-II, we observe an increase in R_{NL} for a high B_\perp (Figs. 5(c),(d)), which is along the lines of a gate-tunable anisotropy in τ_s reported by Benitez *et al.* [15]. In order to confirm the origin of the enhanced R_{NL} , we measure the magnetoresistance (MR) of the encapsulated region as a function of B_\perp and obtain a similar order of change in the graphene-MR. Therefore, we cannot unambiguously determine the presence of an anisotropic spin-relaxation in our system, and additional Hanle measurements as a function of in-plane [14] and oblique magnetic field [15] will be required to draw a conclusion.

According to Cummings *et al.* [11], the anisotropy in the in-plane and out-of plane spin-relaxation can not always be observed. It depends on the intervalley scattering rate and the relative strengths of the in-plane Rashba SOC λ_R induced at the graphene-WS₂ interface due to broken inversion symmetry [3, 4, 11] and the out-of-plane valley-Zeeman SOC λ_V induced in graphene due to the intrinsic SOC in WS₂ [4, 5, 11]. In case of a weak-intervalley scattering, the dominant Rashba SOC gives rise to a faster relaxation of the out-of-plane spins and hinders us from observing a strong anisotropic effect [11]. However, a direct conclusion regarding the intervalley scattering rate cannot be drawn from the spin-transport measurements alone.

Our results also provide an alternative explanation to the observations of refs.[12, 13] where an enhanced spin-signal is observed when the TMD does not conduct. At this point, E_F in graphene is shifted to the hole doped regime. Due to partial encapsulation of graphene via the TMD in refs.[12, 13], the encapsulated and non-encapsulated regions have different spin-transport properties, and the net spin-relaxation rate is dominated by the spin-relaxation at the graphene-TMD interface. It is reflected in a reduced value of ΔR_{NL} and τ_s , coinciding with the conducting-state of the TMD for the electron-doped regime in graphene. Therefore, based on our results, we argue that it is the modulation of the spin-orbit coupling strength than the spin-absorption which changes the spin-relaxation time,

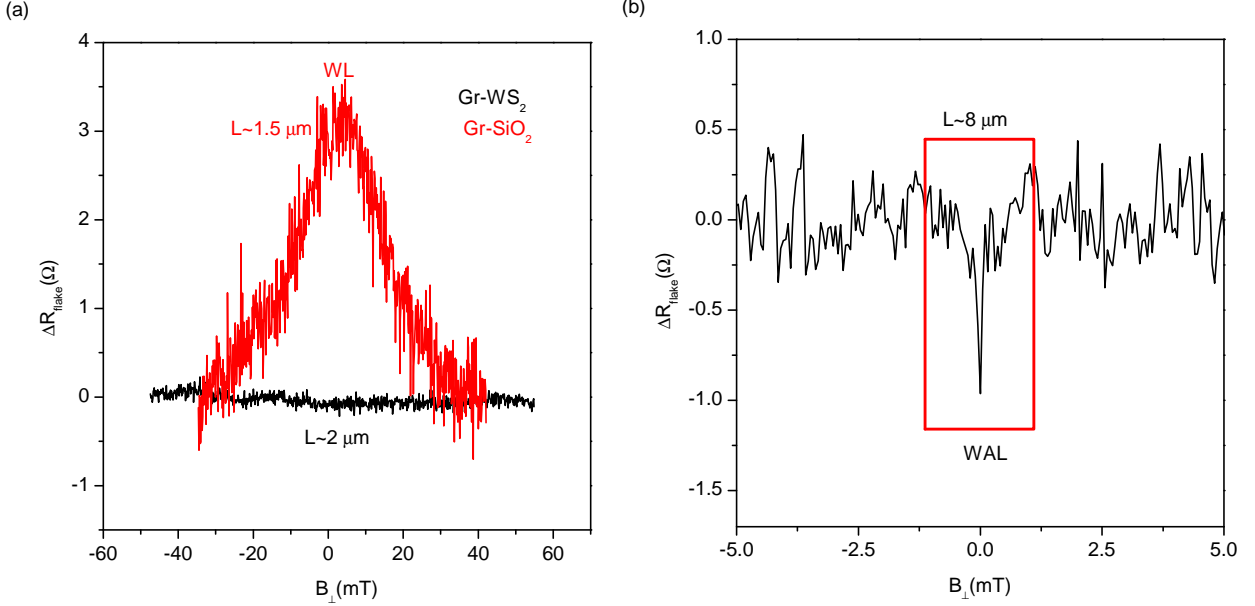


FIG. 7. (a) A WL signal for ref B flake on a SiO₂ substrate (red) and no WL/WAL signature was detected for graphene-on-WS₂ (region-I of stack A). (b) A narrow WAL signature in the encapsulated region was detected due to more spatial averaging in a longer region (region-II of stack A). All the data shown here is taken at 4 K.

leading to the same results.

Alternatively, in order to confirm the presence of a substrate induced SOC in graphene, we perform the quantum magnetoresistance measurements in graphene in the electron-doped regime at 4 K, using the local four-probe geometry. Here we measure the flake resistance as a function of an out-of plane magnetic field with several averaging operations, in order to suppress the universal conductance fluctuations (UCF) in the sample resistance at low temperatures [34]. First, we measure the MR of the reference graphene-flake on SiO₂ (ref B) substrate at 4 K. Here we see a weak-localization (WL) signature (Fig. 7(a)). A WL signature appears at low magnetic fields due to a suppressed back-scattering of electrons [34]. A broad WL signal is probably due to the low mobility of graphene-on-SiO₂. [4, 6, 34]. However, for graphene-on-WS₂ (region-I, stack A) under the same measurement conditions, we do not observe any signature of the weak localization. For graphene-on-WS₂ we have even three times higher mobility than the reference sample which should help in observing a WL peak at a small range of the magnetic field [6]. The absence of the WL signal in graphene-

on-WS₂ indicates the emergence of a competing behavior, for example due to the weak anti-localization effect. In fact, when we measure the MR for a longer graphene-channel of length $\sim 8 \mu\text{m}$, including the encapsulated region, we observe a clear WAL signature (Fig. 7(b)), which could be due to more spatial averaging of the signal in a longer graphene-channel. The observation of the WAL signature in the WS₂ supported single layer graphene confirms the existence of an enhanced SOC in graphene [5, 6].

CONCLUSIONS

In conclusion, we study the effect of a TMD (WS₂) substrate induced SOC in graphene via pure spin-transport measurements. In spin-valve measurements for a broad carrier density range and independent of the conducting state of WS₂, we observe a constant spin-signal, and unambiguously show that the spin-absorption process is not the dominant mechanism limiting the spin-relaxation time in graphene on a WS₂ substrate. The proximity induced SOC reflects in broad Hanle curves with $\tau_s \sim 10\text{-}14$ ps in the electron doped regime. Via the top-gate voltage application in the encapsulated region, we measure $\tau_s \sim 40\text{-}80$ ps in the hole-doped regime, implying a reduced SOC strength. We also confirm the signature of the proximity induced SOC in graphene via WAL measurements. For both electron and hole regimes, we observe the DP-type spin-relaxation mechanism. The presence of the DP-type behavior is more (less) pronounced for the hole (electron) regime due to a higher (lower) τ_s . We also demonstrate the modification of τ_s as a function of an out-of-plane electric field in the hBN-encapsulated region which suggests the control of in-plane Rashba SOC via the electrical gating. In future experiments, in order to realize more effective control of electric field on τ_s , the single layer graphene can be replaced by a bilayer graphene [35, 36]. To enhance the spin-signal magnitude, a bilayer hBN tunnel barrier [8] with a high spin-injection-detection efficiency can also be used.

Summarizing our results, we for the first time, unambiguously demonstrate the effect of the proximity induced SOC in graphene on a semi-conducting WS₂ substrate with high intrinsic SOC via pure spin-transport measurements, opening a new avenue for high mobility spintronic devices with enhanced spin-orbit strength. A gate controllable SOC and thus the modulation of τ_s almost by an order of magnitude in our graphene/WS₂ heterostructure paves a way for realizing the future spin-transistors.

ACKNOWLEDGEMENTS

We acknowledge J. G. Holstein, H. M. de Roos, T. Schouten and H. Adema for their technical assistance. We are extremely thankful to M. Gurram for the scientific discussion and his help during the sample preparation and measurements. This research work was funded from the European Union's Horizon 2020 research and innovation programme (grant no.696656) and supported by the Zernike Institute for Advanced Materials and the Netherlands Organization for Scientific Research (NWO).

* corresponding author; s.omar@rug.nl

- [1] G. Giovannetti, P. A. Khomyakov, G. Brocks, P. J. Kelly, and J. van den Brink, [Phys. Rev. B **76**, 073103 \(2007\)](#).
- [2] C. R. Woods, L. Britnell, A. Eckmann, R. S. Ma, J. C. Lu, H. M. Guo, X. Lin, G. L. Yu, Y. Cao, R. V. Gorbachev, A. V. Kretinin, J. Park, L. A. Ponomarenko, M. I. Katsnelson, Y. N. Gornostyrev, K. Watanabe, T. Taniguchi, C. Casiraghi, H.-J. Gao, A. K. Geim, and K. S. Novoselov, [Nat. Phys. **10**, 451 \(2014\)](#).
- [3] B. Yang, M. Lohmann, D. Barroso, I. Liao, Z. Lin, Y. Liu, L. Bartels, K. Watanabe, T. Taniguchi, and J. Shi, [Phys. Rev. B **96**, 041409 \(2017\)](#).
- [4] B. Yang, M.-F. Tu, J. Kim, Y. Wu, H. Wang, J. Alicea, R. Wu, M. Bockrath, and J. Shi, [2D Mater. **3**, 031012 \(2016\)](#).
- [5] Z. Wang, D.-K. Ki, H. Chen, H. Berger, A. H. MacDonald, and A. F. Morpurgo, [Nat. Commun. **6**, 9339 \(2015\)](#).
- [6] Z. Wang, D.-K. Ki, J. Y. Khoo, D. Mauro, H. Berger, L. S. Levitov, and A. F. Morpurgo, [Phys. Rev. X **6**, 041020 \(2016\)](#).
- [7] S. Omar and B. J. van Wees, [Phys. Rev. B **95**, 081404 \(2017\)](#).
- [8] M. Gurram, S. Omar, and B. J. v. Wees, [Nat. Commun. **8**, 248 \(2017\)](#).
- [9] M. Gmitra and J. Fabian, [Phys. Rev. B **92**, 155403 \(2015\)](#).
- [10] D. Xiao, W. Yao, and Q. Niu, [Phys. Rev. Lett. **99**, 236809 \(2007\)](#).
- [11] A. W. Cummings, J. H. Garcia, J. Fabian, and S. Roche, [Phys. Rev. Lett. **119**, 206601 \(2017\)](#).
- [12] A. Dankert and S. P. Dash, [Nat. Commun. **8**, 16093 \(2017\)](#).

- [13] W. Yan, O. Txoperena, R. Llopis, H. Dery, L. E. Hueso, and F. Casanova, [Nat. Commun. **7**, 13372 \(2016\)](#).
- [14] T. S. Ghiasi, J. Ingla-Aynés, A. A. Kaverzin, and B. J. van Wees, [arXiv:1708.04067 \[cond-mat\] \(2017\)](#), arXiv: 1708.04067.
- [15] L. A. Benítez, J. F. Sierra, W. S. Torres, A. Arrighi, F. Bonell, M. V. Costache, and S. O. Valenzuela, [arXiv:1710.11568 \[cond-mat\] \(2017\)](#), arXiv: 1710.11568.
- [16] A. V. Kretinin, Y. Cao, J. S. Tu, G. L. Yu, R. Jalil, K. S. Novoselov, S. J. Haigh, A. Gholinia, A. Mishchenko, M. Lozada, T. Georgiou, C. R. Woods, F. Withers, P. Blake, G. Eda, A. Wirsig, C. Hucho, K. Watanabe, T. Taniguchi, A. K. Geim, and R. V. Gorbachev, [Nano Lett. **14**, 3270 \(2014\)](#).
- [17] D. Huertas-Hernando, F. Guinea, and A. Brataas, [Phys. Rev. Lett. **103**, 146801 \(2009\)](#).
- [18] C. Ertler, S. Konschuh, M. Gmitra, and J. Fabian, [Phys. Rev. B **80**, 041405 \(2009\)](#).
- [19] M. Gmitra, D. Kochan, P. Högl, and J. Fabian, [Phys. Rev. B **93**, 155104 \(2016\)](#).
- [20] M. Guimarães, P. Zomer, J. Ingla-Aynés, J. Brant, N. Tombros, and B. van Wees, [Phys. Rev. Lett. **113**, 086602 \(2014\)](#).
- [21] P. J. Zomer, M. H. D. Guimarães, J. C. Brant, N. Tombros, and B. J. v. Wees, [Appl. Phys. Lett. **105**, 013101 \(2014\)](#).
- [22] S. V. Morozov, K. S. Novoselov, M. I. Katsnelson, F. Schedin, D. C. Elias, J. A. Jaszczak, and A. K. Geim, [Phys. Rev. Lett. **100**, 016602 \(2008\)](#).
- [23] M. Gurram, S. Omar, S. Zihlmann, P. Makk, C. Schönenberger, and B. J. van Wees, [Phys. Rev. B **93**, 115441 \(2016\)](#).
- [24] N. Tombros, C. Józsa, M. Popinciuc, H. T. Jonkman, and B. J. van Wees, [Nature **448**, 571 \(2007\)](#).
- [25] M. Popinciuc, C. Józsa, P. J. Zomer, N. Tombros, A. Veligura, H. T. Jonkman, and B. J. van Wees, [Phys. Rev. B **80**, 214427 \(2009\)](#).
- [26] M. Isasa, M. C. Martínez-Velarte, E. Villamor, C. Magén, L. Morellón, J. M. De Teresa, M. R. Ibarra, G. Vignale, E. V. Chulkov, E. E. Krasovskii, L. E. Hueso, and F. Casanova, [Phys. Rev. B **93**, 014420 \(2016\)](#).
- [27] F. Volmer, M. Drögeler, T. Pohlmann, G. Gntherodt, C. Stampfer, and B. Beschoten, [2D Mater. **2**, 024001 \(2015\)](#).
- [28] W. Han, R. K. Kawakami, M. Gmitra, and J. Fabian, [Nat. Nanotech. **9**, 794 \(2014\)](#).

- [29] W. Han and R. K. Kawakami, [Phys. Rev. Lett. **107**, 047207 \(2011\)](#).
- [30] C. Józsa, T. Maassen, M. Popinciuc, P. J. Zomer, A. Veligura, H. T. Jonkman, and B. J. van Wees, [Phys. Rev. B **80**, 241403 \(2009\)](#).
- [31] P. J. Zomer, M. H. D. Guimarães, N. Tombros, and B. J. van Wees, [Phys. Rev. B **86**, 161416 \(2012\)](#).
- [32] H. Min, J. E. Hill, N. A. Sinitsyn, B. R. Sahu, L. Kleinman, and A. H. MacDonald, [Phys. Rev. B **74**, 165310 \(2006\)](#).
- [33] M. Gmitra, S. Konschuh, C. Ertler, C. Ambrosch-Draxl, and J. Fabian, [Phys. Rev. B **80**, 235431 \(2009\)](#).
- [34] M. B. Lundeberg, R. Yang, J. Renard, and J. A. Folk, [Phys. Rev. Lett. **110**, 156601 \(2013\)](#).
- [35] J. Y. Khoo, A. F. Morpurgo, and L. Levitov, [Nano Lett. **17**, 7003 \(2017\)](#).
- [36] M. Gmitra and J. Fabian, [Phys. Rev. Lett. **119**, 146401 \(2017\)](#).